Cell-Penetrating Peptides and Peptide Nucleic Acid-Coupled MRI Contrast Agents: Evaluation of Cellular Delivery and Target Binding

Ritu Mishra,[†] Wu Su,[†,#] Rolf Pohmann,[†] Josef Pfeuffer,[†,§] Martin G. Sauer,[‡] Kamil Ugurbil,[†,⊥] and Jörn Engelmann*[,†]

High-Field Magnetic Resonance Center, Max Planck Institute for Biological Cybernetics, Spemannstrasse 41, Tübingen, 72076, Germany, and Pediatric Hematology and Oncology, Hannover Medical School, Hannover, 30625, Germany.
Received February 2, 2009; Revised Manuscript Received July 24, 2009

Molecular imaging of cells and cellular processes can be achieved by tagging intracellular targets such as receptors, enzymes, or mRNA. Seeking to visualize the presence of specific mRNAs by magnetic resonance (MR) imaging, we coupled peptide nucleic acids (PNA) with gadolinium-based MR contrast agents using cell-penetrating peptides for intracellular delivery. Antisense to mRNA of DsRed2 protein was used as proof of principle. The conjugates were produced by continuous solid-phase synthesis followed by chelation with gadolinium. Their cellular uptake was confirmed by fluorescence microscopy and spectroscopy as well as by MR imaging of labeled cells. The cell-penetrating peptide D-Tat$_{57-49}$ was selected over two other derivatives of HIV-1 Tat peptide, based on its superior intracellular delivery of the gadolinium-based contrast agents. Further improved delivery of conjugates was achieved upon coupling peptide nucleic acids (antisense to mRNA of DsRed2 protein and nonsense with no natural counterpart). Significant enhancement in MR contrast was obtained in cells labeled with concentrations as low as 2.5 μM of these agents. Specific binding of the targeting PNA containing conjugate to its complementary oligonucleotide sequence was proven by *in vitro* cell-free assay. In contrast, a lack of specific enrichment was observed in transgenic cells containing the target due to nonspecific vesicular entrapment of contrast agents. Preliminary biodistribution studies showed conjugate-related fluorescence in several organs, especially the liver and bladder, indicating high mobility of the agent in spite of its high molecular weight. No conjugate related toxicity was observed. These results are encouraging, as they warrant further molecular optimization and consecutive specificity studies *in vivo* of this new generation of contrast agents.

INTRODUCTION

Recently, remarkable progress in the understanding of cellular processes, at both the molecular and genetic levels, has been made by the development of molecular-biological assays. Despite this, a myriad of questions about biological processes under normal as well as diseased conditions remain. Of late, the new field of molecular imaging has evolved with the intent of translating knowledge gained from *in vitro* systems into studies of complete biological systems. Molecular imaging aims at noninvasive visualization of biological processes amid the complex networks and interactions in the intact individual (*1*−*3*). Imaging modalities being extensively used for this purpose are positron emission tomography (PET), single-photon emission computed tomography (SPECT), optical imaging using fluorescence or bioluminescence, and magnetic resonance imaging (MRI) (*4, 5*).

* To whom correspondence should be addressed: Jörn Engelmann. High-Field Magnetic Resonance Center, Max Planck Institute for Biological Cybernetics, Spemannstrasse 41, Tübingen, 72076, Germany. E-mail: joern.engelmann@tuebingen.mpg.de; Tel: +49-7071-601704; Fax: +49-7071-601702.

[†] Max Planck Institute for Biological Cybernetics.

[‡] Hannover Medical School.

[#] Present address: Department of Chemistry, University of Leicester, Leicester, LE17RH, U.K.

[§] Present address: Siemens Medical Solutions USA, Inc., Charlestown, MA 02129, USA.

[⊥] Present address Center for Magnetic Resonance Research, University of Minnesota, Department of Radiology, Minneapolis, MN 55455, USA.

MRI is a powerful tool in clinical diagnostics as well as for understanding developmental and biological processes. It visualizes the differences in tissues and organs, as well as between normal and pathological changes, as a function of water concentration and relaxation times, T_1 and T_2, in a given volume element (*6*). The main advantages of MRI over other imaging techniques are its high spatial and temporal resolution, the absence of harmful ionizing radiation, and the ability to noninvasively scan entire organisms in one, two, or three dimensions. The intrinsic contrast of MR images can be augmented by the use of contrast agents (CAs). Chelated paramagnetic metal ions, in particular gadolinium, have been primarily used as T_1-based CAs to increase the contrast in MR images (*7*). An assortment of gadolinium-based CAs are commercially available, and these agents are frequently employed for clinical diagnosis. However, their utility is based on enhancement of anatomical information due to differential biodistribution in the body (*8, 9*). For example, in the brain, these agents do not cross the blood−brain barrier (BBB) except when the BBB is broken because of pathology; as such, they lack specificity. Advancing from these agents toward extracellular targeting by conjugation of CAs to certain proteins and especially to monoclonal antibodies or antibody fragments has been explored. Most of the investigations were related to the development of tumor-specific agents (*10*−*14*).

Numerous intracellular imaging targets are available, however, and these can be tagged to provide molecular information. Regardless of the low number of targets at DNA level, molecules at RNA (overexpressed) or protein level could serve as potential targets (*1*). A possibility for monitoring gene expression by targeting a tumor-specific mRNA was evaluated by Heckl et

10.1021/bc9000454 CCC: $40.75
Published on Web 09/29/2009

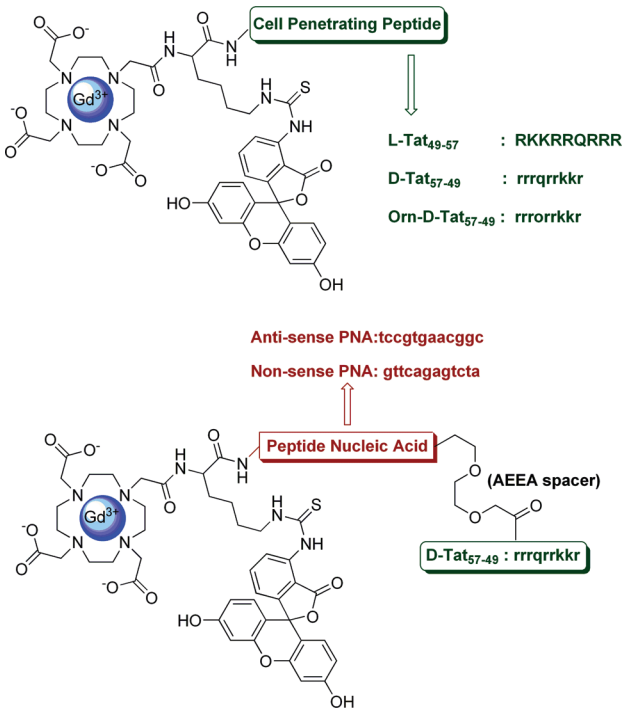

Figure 1. Schematic structures of CPP and PNA conjugated Gd(DOTA) based intracellular contrast agents. All amino acids are represented in a single letter code: R, arginine; K, lysine; Q, glutamine; and O, ornithine. D-Amino acids are represented in lower case. The PNA building blocks are represented as follows: a, adenine; t, thymine; g, guanine; c, cytosine.

al. (*15*). Our group has also reported the development of a gadolinium-based CA coupled to peptide nucleic acids (PNA) to target mRNA (*16*). Both studies utilized peptide-based delivery of their constructs to penetrate through the cell membrane. Such cell-penetrating peptides (CPPs) emerged as an extremely efficient way to overcome the most challenging delivery barrier. CPPs are a class of short peptides that have been reported to import a wide range of cell-membrane impermeable cargos into cells (*17*−*20*). Thus far, there is no consensus on the mechanism of uptake of CPPs and the maintenance of functionality of cargos after delivery. This is reflected by differences in reported labeling techniques, non-standardized protocols regarding uptake evaluation, and discrepancies caused by the use of different cellular model systems (*21*−*23*).

Keeping these issues in mind, we began by evaluating the most appropriate CPP, selected from three derivatives of the well-established CPP HIV-1 Tat peptide, to deliver CA into cells. The cargo attached to the CPP was a gadolinium-loaded chelator, 1,4,7,10-tetraazacyclododecane-*N*,*N*′,*N*″,*N*‴-tetraacetic acid (Gd-DOTA), for MR imaging, and fluorescein isothiocyanate (FITC) for optical imaging (Figure 1). Using the selected CPP, a targeting PNA (either targeting DsRed2 mRNA or a nonsense sequence) was introduced into the above-mentioned conjugate (Figure 1). DsRed2 protein, a variant of the DsRed protein, was used as a model system for proof-of-principle in a transgenic DsRed2-expressing cell line (*24*). The aim was to assess the intracellular delivery and distribution of these larger molecules in the presence or absence of target mRNA in the cells. The ability of the agents to bind with targets in a cell-free *in vitro* system, as well as by labeling cells, was also evaluated. The biodistribution of the CA containing the antisense PNA will also be briefly presented here using fluorescence for detection.

EXPERIMENTAL PROCEDURES

General. All chemicals were purchased at HPLC or peptide synthesis grade from commercial sources. Trifluoroacetic acid (TFA), dimethylformamide (DMF), dichloromethane (DCM), *N*,*N*-diisopropylethylamine (DIEA), triisopropylsilane (TIPS), methyl tertiary butyl ether (MTBE), and FITC were obtained from Acros Organics (Germany). All standard, protected Fmoc amino acid derivatives (the side chains of lysine and ornithine were protected by Boc and arginine by Pbf), 2-(1-*H*-benzotriazol-1-yl)-1,1,3,3-tetramethyluronium hexafluorophosphate (HBTU), preloaded Wang resin, and 1-hydroxybenzotriazole (HOBt) were purchased from Novabiochem, United Kingdom. For PNA synthesis, all Fmoc/Bhoc protected monomers and 2-(1-*H*-7-azabenzotriazole-1-yl)-1,1,3,3-tetramethyluronium hexafluorophosphate (HATU) were purchased from Applied Biosystems, Germany. 1,4,7,10-Tetraazacyclododecane (cyclen) was purchased from Strem Chemicals, France.

Analytical and semipreparative RP-HPLC was performed at room temperature on a Varian PrepStar Instrument (Australia) equipped with PrepStar SD-1 pump heads. UV absorbance was measured using a ProStar 335 photodiode array detector at 260 nm. A Varian Polaris C18-Ether column (4.6 × 250 mm, particle size 5 μm, particle pore diameter 100 Å) was used for analytical RP-HPLC. For semipreparative HPLC, a Varian Polaris C18-Ether column (21.2 × 250 mm, 5 μm, 100 Å) was used.

Gd-DOTA-conjugated CPPs and PNAs were analyzed and purified using one of the following two methods. Method A: A linear gradient was used starting from 90% solvent A (0.1% TFA in water) and 10% of solvent B (0.1% TFA in acetonitrile) to 90% B in 30 min. Method B: A linear gradient was used starting from 90% solvent A (0.05% TFA in water) and 10% of solvent B (0.05% TFA in acetonitrile) to 90% B in 30 min (flow rate of 1 mL/min for analytical and 3 mL/min for semipreparative HPLC).

ESI-MS was performed on Agilent SL 1100 Series LC/MSD Trap system (Agilent, Germany): nebulizer, 20.0 psi; dry gas, 5.0 L/min; dry temperature, 250 °C.

General Synthesis of Gd-DOTA-CPP(FITC) Conjugates. All the CPPs used in this work were chemically synthesized by solid-phase peptide synthesis with Fmoc/*t*Bu-strategy on a Heidolph Synthesis 1 synthesizer (Germany). As shown in Scheme 1, polystyrene-based Wang resin (substitution level of 0.50−0.60 mmol/g) was swollen in DCM for 30 min and washed four times with DMF. The resin was treated twice with a solution of 20% piperidine (3 mL) in DMF for 10 min, and subsequently washed four times with DMF. In a separate vial, Fmoc-protected amino acid (4 equiv), HBTU (3.6 equiv), and HOBt (3.6 equiv) were dissolved in DMF (2 mL), and DIEA (8 equiv) was added. The resulting solution was added to the resin and allowed to react under N_2 for 30 min. The resin was drained and rinsed four times with DMF. This procedure was repeated until Fmoc-protected CPPs (L-Tat$_{49-57}$, D-Tat$_{57-49}$, and Orn-D-Tat$_{57-49}$ peptides) bound to Wang resin were obtained. The resin-bound peptides were deprotected with 20% piperidine (3 mL) in DMF for 10 min, and coupled with one Fmoc-Lys(Dde)−OH residue by using HBTU and HOBt coupling agents. After deprotection with 20% piperidine (3 mL) in DMF for 10 min, in-house synthesized DOTA (*tert*-butyl)$_3$ ester was coupled to the α-NH_2 group of Lys (coupling condition: DOTA (*tert*-butyl)$_3$/HATU/DIEA = 4:3.6:8) (*16*). The resin was drained and rinsed four times with DMF. The resin-bound DOTA-conjugated L-Tat$_{49-57}$, D-Tat$_{57-49}$, and Orn-D-Tat$_{57-49}$ peptides were treated twice with hydrazine hydrate (2% in DMF, 2 min) to remove the Dde group. The ε-amino group of N-terminal

Scheme 1. Synthesis of CPP Conjugated MR Contrast Agents by Continuous Solid-Phase Synthesis

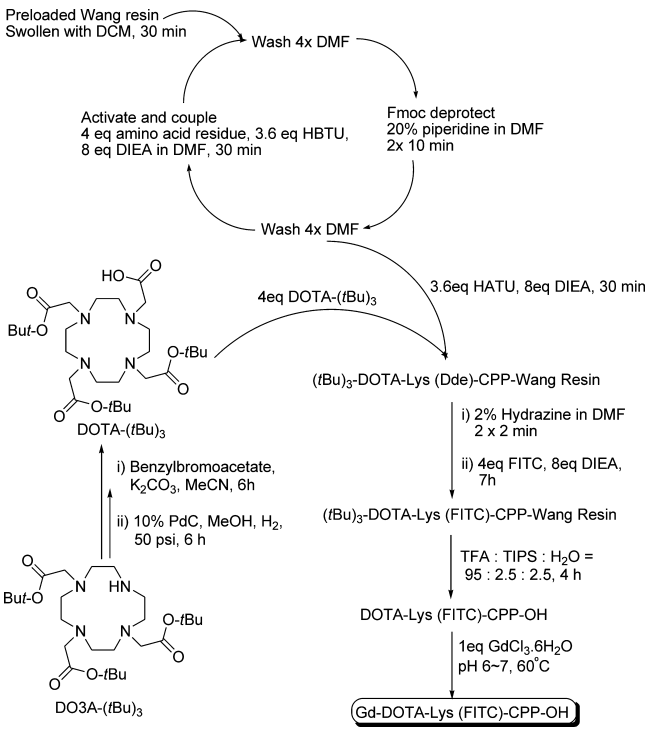

lysine was manually labeled with FITC (4-fold excess) mixed with triethylamine (1:2) in DMF overnight. The solvent was removed and the resin was washed with DMF, DCM, and MeOH subsequently four times. After drying under vacuum, DOTA-Lys(FITC)-conjugated peptides (L-Tat_{49-57}, D-Tat_{57-49}, and Orn-D-Tat_{57-49}) were cleaved off the resin using TFA/TIPS/H_2O (95:2.5:2.5, v/v/v). In the entire procedure described above, completion of Fmoc deprotection, coupling and thiourea formation were monitored by Kaiser Test (*25*).

Purification. All peptide conjugates were precipitated with cold MTBE. The precipitates were collected by centrifugation and resuspended in cold MTBE two times. Pellet was dissolved in water and *tert*-butyl alcohol (1:4) with 2% acetic acid, and lyophilized. All crude samples were purified by semipreparative RP-HPLC using linear gradients as described in the General Experimental Procedures before. The product-containing fractions were defined by analytical RP-HPLC.

Preparation of Gd Complexes. The ligands (DOTA-conjugated FITC-labeled CPPs) were dissolved in 5 mL water; a solution of $GdCl_3 \cdot 6H_2O$ (1 equiv) in water was added and the pH was periodically adjusted to 6.0−7.0 using a solution of 1 N NaOH or 1 N HCl as needed. The residues were purified by semipreparative RP-HPLC using method B to separate unstably bound Gd^{3+}. Afterward, the product was dialyzed (Float-ALyzer, cellulose ester membranes, MWCO 1000; Spectrum Laboratories Inc., Germany) to remove inorganic impurities. The solutions were lyophilized, and yellowish orange solids were obtained. The absence of free Gd^{3+} was checked with xylenol orange indicator (*26*).

Gd-DOTA-Lys(FITC)-L-Tat_{49-57}-OH. ESI-MS (+): calcd *m/z* 2397.08; found 800.2[$(M + 3H)^{3+}$], 600.2 [$(M + 4H)^{4+}$], 480.4 [$(M + 5H)^{5+}$], and 400.5 [$(M + 6H)^{6+}$].

Gd-DOTA-Lys(FITC)-D-Tat_{57-49}-OH. ESI-MS (+): calcd *m/z* 2397.08; found 799.7 [$(M + 3H)^{3+}$], 600.2 [$(M + 4H)^{4+}$], 480.3 [$(M + 5H)^{5+}$], and 400.7 [$(M + 6H)^{6+}$].

Gd-DOTA-Lys(FITC)-Orn-D-Tat_{57-49}-OH. ESI-MS (+): calcd *m/z* 2383.10; found 796.2 [$(M + 3H)^{3+}$], 596.5 [$(M + 4H)^{4+}$], 477.7 [$(M + 5H)^{5+}$], and 398.4 [$(M + 6H)^{6+}$].

Two PNA-containing conjugates, anti-dsred CA and nonsense CA were synthesized using the same synthetic scheme as reported before (*16*). In brief, PNA building blocks were coupled through an AEEA spacer to D-$Tat_{(57-49)}$ by a continuous solid-phase synthesis scheme. On completion of the PNA sequence, a Fmoc and Dde protected Lys residue was conjugated. DOTA tris(*tert*-butyl) ester was synthesized in-house (*27*) and coupled to the Lys on its α-NH_2 group after deprotection of Fmoc. Next, FITC was conjugated with the ε-NH_2 group of the Lys. The conjugates were cleaved off the resin and loaded with gadolinium under mild conditions. After purification by HPLC and dialysis, the products were characterized by ESI-MS.

Concentration Estimation. Peptide conjugates were dissolved in Milli-Q water to obtain a 10 mM solution by weight. For the determination of the real concentration, these stock solutions were diluted 1:100 in Dulbecco's Modified Eagle's Medium (DMEM; Biochrom AG, Germany). The absorbance of the solutions was measured in a multiplate reader (BMG Labtech, Germany) at 485 nm with ratiometric correction of turbidity at 690 nm. The concentrations of the stock solutions were calculated assuming $\varepsilon_{\text{carboxyfluorescein } 485 \text{ nm}} = 81\,000$ L/(mol·cm), and all further dilutions were done according to this calculated concentration.

Cell Culture. NIH 3T3 cells were obtained from DSMZ, Germany, CCL-11 fibrosarcoma cells from ATCC, USA, and the DsRed2 protein-expressing fibrosarcoma CCL-11 cell line (DsRed cells) was a kind gift of Dr. Marna Ericsson, University of Minnesota, USA. NIH 3T3 mouse fibroblasts were cultured as a monolayer at 37 °C with 10% CO_2 in DMEM supplemented with 10% fetal bovine serum (FBS), 4 mM L-glutamine, 100 μg/mL streptomycin, and 100 U/mL penicillin (all purchased from Biochrom AG, Germany). Cultures of DsRed cells and the parent cell line CCL-11 were maintained at 37 °C with 5% CO_2 in NCTC 135 medium (Sigma, Germany) supplemented with 10% heat-inactivated fetal horse serum, 2.2 g/L sodium bicarbonate, and pH adjusted to 7.2. All cells were passaged by trypsinization with trypsin/EDTA 0.05/0.02% (w/v) in phosphate-buffered saline (PBS; Biochrom AG, Germany) every second to third day.

***In Vitro* Binding Assay.** The *in vitro* proof of specific binding of anti-dsred CA was obtained in a cell-free FITC immunoassay with slight modifications (*28*). A synthetic 45-mer single-stranded deoxynucleotide sequence containing the complementary target site of anti-dsred CA was obtained commercially (Eurofins MWG, Germany). The target oligodeoxynucleotide sequence extended by a 12-mer C linker was immobilized on DNA binding plates (Corning, Germany) in DNA binding buffer (50 mM sodium phosphate, 1 mM EDTA, pH 8.5) at 4 °C for 24 h. After washing off excess oligodeoxynucleotide with PBS, the plates were incubated with blocking buffer (DNA binding buffer containing 10% FBS and 3% bovine serum albumin (BSA)) for 2 h at 37 °C. Following a PBS wash, incubation with 16 nM of either anti-dsred CA or nonsense CA in 10 mM sodium phosphate, pH 6.5 was performed. For hybridization, the binding temperature was maintained at 60 °C for 1 h and then slowly decreased to 37 °C for another 1 h. The plates were left overnight at room temperature. The following day, plates were washed 3 times for 5 min each with wash buffer (PBS containing 0.01% Tween). Incubation with an anti-FITC-horseradish peroxidase (HRP)-conjugated antibody (Invitrogen, Germany) was carried out. Subsequent to thorough PBS washing to remove unbound antibody, the signal was developed with tetramethyl benzidine for 30 min at room temperature and absorbance was measured at 650 nm in a multiplate reader (BMG Labtech, Germany). Experiments were run at least three

times for each CA with two replicates. Statistical analysis was performed by Student's *t*-test. *P* values < 0.05 were considered significant.

Cellular Uptake Assay. Internalization experiments on cells were performed in 96 well microplates. At 70−80% confluency, cells were incubated with different concentrations of peptide-coupled CAs in complete culture medium for additional 18 h at routine culture conditions. After incubation, the labeling CAs were removed and cells were incubated with Bisbenzimid 33342 (Hoechst 33342), a nuclear stain, in order to assess the DNA content per well (correlates to the number of cells) (*29, 30*). Cells were washed with HBSS (Biochrom AG, Germany) and extracellular fluorescence was quenched by incubation with cold trypan blue (0.05% (w/v) in PBS) for 3 min followed by repeated washes with HBSS (*31*). Cell-related FITC fluorescence (Ex 485 nm/Em 530 nm) and cell number (Ex 346 nm/Em 460 nm) was evaluated in the multiplate reader. Experiments were run at least three times for each CA with six replicates. Statistical analysis was performed by ANOVA with Tukey's post test. *P* values < 0.05 were considered significant.

Microscopy. The cells in plates processed for fluorescence spectroscopic measurement, as mentioned above, were used for complementary fluorescence microscopy. Microscopy was performed without fixation using a Zeiss Axiovert 200 M microscope (Germany) with an LD Plan NeoFluor 40× objective. For high-resolution microscopy, 5×10^5 cells/mL were cultured on channel slides (Ibidi, Germany) for 24 h. Then, cells were incubated with CA in culture medium for another 18 h under normal culture conditions. These cells were subjected to nuclear staining and trypan blue quenching followed by extensive washing with HBSS. Images were made using a Zeiss Plan APOCHROMAT 63×/1.4 oil DIC objective. OptiGrid (Improvision, England), a structured light device, was used for acquiring images of confocal quality, and Volocity Acquisition and Visualization software (Improvision, England) was used for high-speed image capture and high-resolution rendering of data sets as images or movies. The imaging conditions were kept constant for the observation of all the different samples. Cellular localization and distribution of the peptide was observed by irradiating with blue light (Ex 470/40 nm) and observing at Em 525/50 nm. Apart from FITC fluorescence, the nuclear labeling by Hoechst was observed by Ex 365/15 nm and Em 460/50 nm and trypan blue fluorescence viewed by Ex 535/50 and Em 645/75 nm. Also, phase contrast images with differential interference contrast (DIC) microscopy of the same area were made to observe whether the cells maintain their normal morphology in the presence of CAs.

MR Measurement in Cells. For MR imaging of cells, exponentially growing cells were labeled with different concentrations of CAs in 175 cm^2 tissue culture flasks for 18 h. After repeated washes with HBSS, cells were trypsinized, centrifuged, and resuspended in 1.5 mL Eppendorf tubes at 2×10^7 cells for DsRed and CCL-11 in 500 μL complete medium. Cells were allowed to settle before MR measurements. Tubes with medium only and cells without CA were used as controls.

MR imaging of the cell pellets at room temperature (~21 °C) was performed in a 3 T (123 MHz) human MR scanner (MAGNETOM Tim Trio, Siemens Healthcare, Germany), using a 12-channel RF head coil and slice-selective measurements from a slice with a thickness of 1 mm positioned through the cell pellet.

T_1 was measured using an inversion−recovery sequence, with an adiabatic inversion pulse followed by a turbo−spin−echo readout. Between 10 and 15 images were taken, with the time between inversion and readout varying from 23 to 3000 ms. With a repetition time of 10 s, 15 echoes were acquired per scan and averaged six times. For T_2, a homewritten spin−echo sequence was used with echo times varying from 19 to 1000 ms in about 10 steps and a repetition time of 8 s. Diffusion sensitivity was reduced by minimizing the crusher gradients surrounding the refocusing pulse. All experiments scanned 256^2 voxels in a field-of-view of 110 mm in both directions resulting in a voxel volume of $0.43 \times 0.43 \times 1$ mm^3.

Data analysis was performed by fitting to relaxation curves with self-written routines under *MATLAB 7.1 R14* (The Mathworks Inc., United States). The series of T_1 and T_2 relaxation data were fitted to the following equations:

$$T_1 \text{ series with varying } t = T_I\text{: } S = S_0(1 - \exp(-t/T_1)) + S(T_I = 0)\exp(-t/T_1) \quad \text{(a)}$$

$$T_2 \text{ series with varying } t = TE\text{: } S = S_0 \exp(-t/T_2) \quad \text{(b)}$$

Nonlinear least-squares fitting of three parameters S_0, $S_{(TI = 0)}$, and T_1/T_2 was done for manually selected regions of interest with the Trust Region Reflective Newton algorithm implemented in *MATLAB*. The quality of the fit was controlled by visual inspection and by calculating the mean errors and residuals.

Biodistribution Study. C57BL/6 mice were used to study the *in vivo* distribution of anti-dsred CA. The CA was injected intravenously via the tail vein at a dose of 10 μmol/kg in 100 μL saline. An equivalent volume of saline was injected into the control animal. After 20 min, animals were sacrificed and biodistribution was assessed. Tissues harvested included lungs, liver, spleen, kidney, heart, bladder, and brain. All tissues were rinsed with PBS to remove blood or hair, and a slice of arbitrary thickness from each tissue was placed on a glass slide for microscopic observation. Microscopy was performed using a Zeiss EC Plan-NEOFLUOR 20×/0.5 objective. Fluorescence and bright field images of the tissues were obtained and observed for CA-related FITC fluorescence.

RESULTS AND DISCUSSION

Evaluation of Optimal CPP. Among the increasing number of transduction peptides that are being characterized, HIV-1 Tat and polyarginines represent two of the particularly well studied. Over the years, more efficient sequences have been derived by modifications of Tat CPP (*32, 33*). Although polyarginines were the foremost to be used for intracellular delivery of CAs (*34*), of late a higher toxicity of polyarginines has been suggested in comparison to Tat (*35*). Therefore, we decided to evaluate the efficiency of three HIV-1 Tat derivatives to translocate MR CAs together with FITC into cells. Thus far, there are only a few publications about the use of HIV-1 Tat to transport CAs for MRI (*36*−*38*). Large amounts of CA need to be transported into cells to obtain maximum MR contrast enhancement because of the low sensitivity of MRI. Therefore, we chose long incubation times. On the other hand, labeling protocols more close to *in vivo* conditions were applied using incubation in the presence of culture medium containing serum instead of serum-free buffer formulations and an incubation temperature of 37 °C. We observed that in the presence of serum the rate of uptake was slowed down (data not shown). This might be due to an interaction of the conjugates with serum components. A routine laboratory embryonic mouse fibroblasts cell line NIH 3T3 was selected for comparison of uptake efficiency.

We synthesized the Gd-DOTA-Lys(FITC) conjugates of L-$Tat_{(49-57)}$ (L-Tat CA), D-$Tat_{(57-49)}$ (D-Tat_{inv} CA), and Orn-D-$Tat_{(57-49)}$ (substitution of the glutamine residue with ornithine) (Orn-D-Tat_{inv} CA) in-house (*32*) (Figure 1). Peptide segments were synthesized by an online solid-phase synthesis scheme. Using an additional lysine as linker, DOTA tris(*tert*-butyl) ester was coupled on its α-NH_2 group and FITC on the ε-NH_2 group.

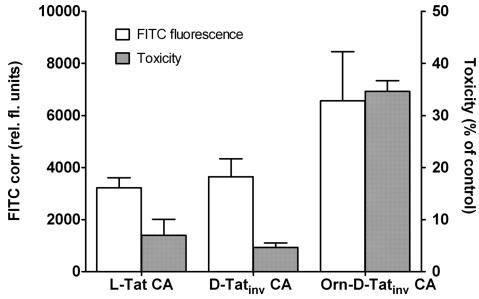

Figure 2. CA related fluorescence measured by fluorescence spectroscopy in NIH 3T3 embryonic mouse fibroblast cells. Cells were incubated with contrast agents at a concentration of 20 μM in complete medium for 18 h. External fluorescence was quenched with trypan blue and subsequent washes with HBSS. Values are means ± SEM; $n = 3$ with six replicates each.

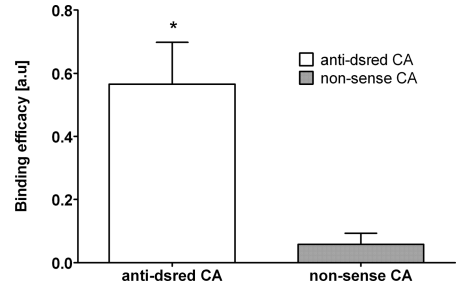

Figure 3. Binding efficacy of anti-dsred and nonsense CA in an *in vitro* binding assay. Synthetic single-stranded target DNA was immobilized on DNA binding plates, and nonspecific binding sites were blocked with BSA/FBS. Hybridization was performed with anti-dsred and nonsense CA, followed by extensive washing to eliminate nonspecific binding. Detection by anti-FITC-HRP-conjugated antibody. Values are means ± SEM, $n = 3$ with two replicates each. *: $p < 0.05$ statistically significantly different between contrast agents, Student's *t*-test.

The final gadolinium-loaded compounds were used to label cells. Fluorescence spectroscopy was applied to assess cellular uptake by FITC fluorescence and toxicity by nuclear DNA content estimation after staining with Hoechst 33342 (*29, 30*).

Of the three sequences tested, Orn-D-Tat$_{(57-49)}$ was the most efficient in delivering the conjugates across the cell membrane (Figure 2). However, its uptake was accompanied by a significant reduction of DNA content (directly correlated to the number of cells), thus limiting its exploitation. Our results did not reveal much difference in the uptake of conjugates with L-Tat$_{(49-57)}$ or D-Tat$_{(57-49)}$, both of which had negligible toxicity (although D-Tat$_{(57-49)}$ has been reported to be a more efficient transporter for other cargos (*39*)). This difference could be attributed to the influence of the Gd-loaded chelate on the molecular charge or three-dimensional conformation of the conjugate. Furthermore, it is well-established that D-isomers of amino acids are resistant to enzymatic cleavage and remain longer in the circulation (*39*). Thus, we chose D-Tat$_{(57-49)}$ as the CPP for experiments on further coupling of PNA sequences together with Gd-DOTA and FITC to obtain bimodal targeting agents.

Design and Synthesis of mRNA-Targeted CA. PNA was selected to target unique mRNA sequences. These polyamide nucleic acids are reported to be resistant to enzymatic cleavage in biological fluids and hybridize with DNA or RNA with high specificity and affinity (*40*). As per the base pairing rule, these PNA could bind sequences in cellular mRNA and, therefore, serve as high-affinity probes for molecular imaging. Although most mRNAs are expressed at low copy numbers under normal conditions (50−1000 per cell at any particular time point), these numbers increase manyfold in certain situations like disease or stress (*1*). The use of PNA for imaging specific mRNA could potentially serve for early detection of anomalies by monitoring molecular processes. Because PNAs have poor cellular uptake, they need to be coupled to delivery agents such as CPPs in order to pass through the biological membrane and interact with the intracellular target (*41*).

The intention of our study was to design a multimodal probe by the use of a facile building block approach. The blocks could easily be altered according to the target requirement without significant modification in the synthetic scheme. The molecule eventually designed contained MR and optical imaging moieties linked to PNA for targeting and CPP for intracellular transport. In order to establish proof of principle, mRNA from a variant of the red fluorescent protein, DsRed2, was chosen as the target. Through a BLAST database search, a 12mer antisense sequence (tcc gtg aac ggc, anti-dsred) specific to the DsRed2 mRNA was identified (*16*). Another sequence (gtt cag agt cta) that did not correspond to any known mammalian gene was selected as the nonsense control sequence (*16*).

Two PNA-containing conjugates, anti-dsred CA and nonsense CA, were synthesized using the same synthetic scheme as reported before (*16*) (Figure 1). The chelation of gadolinium in the macrocyclic chelator was confirmed by relaxivity measurements of CA in aqueous solutions. The relaxivity values for both the CAs (2.8 ± 0.3 $mM^{-1}s^{-1}$ for antisense CA and 4.3 ± 0.2 $mM^{-1}s^{-1}$ for nonsense CA) corresponded with values for compounds with one DOTA complexed gadolinium.

***In Vitro* Proof for Binding Specificity of Antisense CA.** The hybridization properties of PNA are crucial for specific antisense targeting. It is established that oligonucleotides of 12 or more bases are adequate for targeting unique genomic sequences (*42*). The targeting specificity of anti-dsred CA in comparison to nonsense CA was determined *in vitro* using a synthetic single-stranded oligodeoxynucleotide sequence (45-mer) as described in Experimental Procedures. Significant specific binding of the antisense CA to the synthetic target was observed (Figure 3). The nonsense counterpart almost completely failed to bind, such that the hybridization signal obtained can be mainly ascribed to specific binding. Thus, *in vitro* studies clearly demonstrated the applicability of the selected antisense PNA sequence for mRNA targeting. Gel retardation studies further verified the specific binding affinity of the antisense CA compared to the nonsense CA (data shown in Supporting Information). A retarded mobility of only the synthetic single-stranded DNA hybridized with the antisense PNA was observed, while the unhybridized DNA and DNA incubated with nonsense PNA showed no change in mobility.

Cellular Uptake and Internalization Studies. CPPs have been used for the delivery of a vast variety of biomolecules. The ability of D-Tat$_{(57-49)}$ to transport our covalently conjugated PNAs along with the imaging moieties was next investigated in whole cells. Murine fibrosarcoma cells transfected with the DsRed2 gene, referred to as DsRed cells (*24*), and their parent cell line CCL-11 were used for internalization assessment by fluorescence spectroscopy and microscopy.

The antisense CA as well as the nonsense CA very efficiently labeled DsRed cells (Figure 4a). Both CAs showed a concentration-dependent transfer into cells up to a labeling concentration of 5 μM. Saturation in internalization was observed at labeling concentrations of >2.5 μM, and a further dose increase was accompanied by increased toxicity but only a marginal improvement in cellular delivery. Thus, for subsequent studies a labeling concentration of 2.5 μM of the PNA-containing CA was used. A comparable uptake profile for both CAs was observed in the nontarget containing CCL-11 cells (data not shown).

Additionally, observations of DsRed and CCL-11 cells by fluorescence microscopy revealed similar uptake and distribution for both the PNA-containing CAs (Figure 4b). These agents

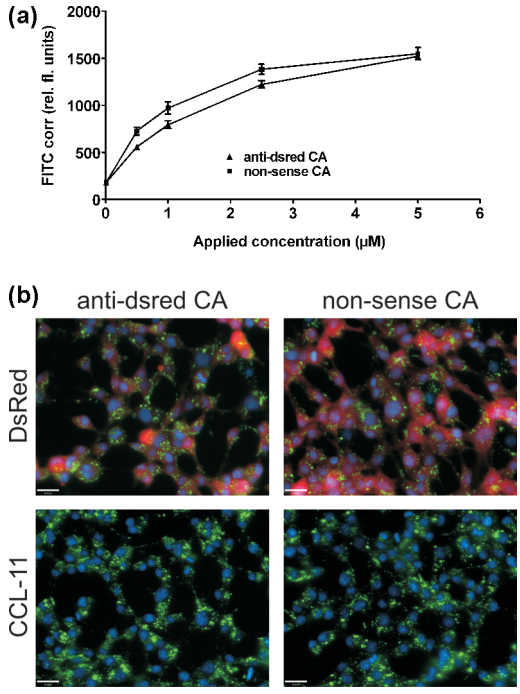

Figure 4. Internalization of anti-dsred and nonsense CA in DsRed and CCL-11 mouse fibrosarcoma cells. Fluorescence spectroscopy (a) and microscopy (b) were performed on cells incubated with 2.5 μM of either anti-dsred or nonsense CA for 18 h. External fluorescence was quenched with trypan blue and subsequent washes with HBSS; values are means $\pm$ SEM, $n = 3$ with six replicates each. The bar represents 20 μm.

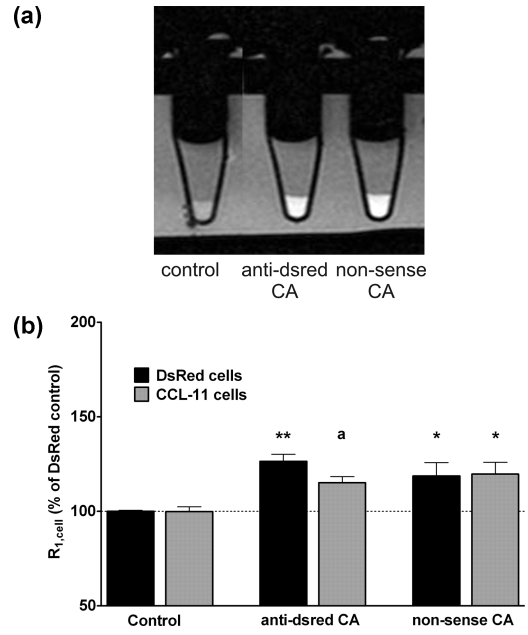

Figure 5. T_1-weighted MR images of DsRed cells after loading with 2.5 μM of anti-dsred and nonsense CA for 18 h (a). Cellular relaxation rate $R_{1,cell}$ in DsRed and CCL-11 cells after labeling with anti-dsred or nonsense CA (b). After treatment with DsRed CA for 18 h, cells were trypsinized, centrifuged, and resuspended in 1.5 mL Eppendorf tubes at 2×10^7 cells/500 μL in complete medium for MR studies. The measured relaxation rates were plotted vs the applied extracellular labeling concentration. Control: cells incubated with culture medium without CA. Values are means $\pm$ SEM; $n = 3$ with two replicates each. *: $p < 0.05$, **: $p < 0.01$ statistically significantly different to control. a: $p < 0.05$ statistically significantly different between cell lines, ANOVA with Tukey's post test.

were distributed in the perinuclear area as bright punctuate dots in both cell lines. This indicates that, despite the difference in the base composition of the two PNA sequences, both antisense and nonsense CA have similar cellular internalization efficacy and properties.

In our study, therefore, the feasibility of using D-Tat$_{(57-49)}$ as a transport vector for large-sized cargos has again been demonstrated. In fact, efficiency similar to that of the D-Tat$_{inv}$ CA was observed when an almost 10 times lower labeling concentration of the PNA-containing CAs was used. Attaching PNA to D-Tat$_{inv}$ largely increased the molecular weight and also raised the hydrophobic nature of the conjugates. We hypothesize that the CPP-PNA CAs might interact better with the cell membrane and hence enhance uptake. The high hydrophobicity of the conjugates containing PNA also reduced their solubility in water. Therefore, the PNA-containing conjugates could be used only at low micromolar concentrations for labeling cells.

Enhancement of MR Contrast in Cells. Previously, we reported that CPP-PNA CAs were highly efficient intracellular CAs yielding contrast enhancement in NIH 3T3 cells at concentrations as low as 0.5 μM (*16*). The possibility to utilize these PNA-containing conjugates as MR contrast-enhancing agents in target-containing cells has now been assessed. Cells producing target mRNA as well as nontarget expressing cells were labeled with 2.5 μM of either the antisense CA or nonsense CA. Cells were labeled for 18 h followed by repeated washings with Hank's buffered saline solution (HBSS, Biochrom AG, Germany). After trypsinization, an average of 2×10^7 cells were transferred into Eppendorf tubes for T_1 and T_2 measurements. Cells were also treated in a similar way but in the absence of any contrast agent to establish background control values.

In agreement with our earlier observations, both conjugates showed significant contrast enhancement in cells (*16*). The T_1 relaxation times in DsRed cells were substantially altered by the nonsense as well as antisense CA at concentrations as low as 2.5 μM (Figure 5a). Remarkably, this labeling concentration was 20−1000 times lower than the amount of CPP linked Gd-based chelators used for delivery into cells (*14, 15, 34, 36, 43*). T_1-weighted images of CCL-11 cells showed similar contrast changes at these low concentrations. The extended incubation times used for CA delivery into cells could be the reason this low concentration is sufficient for significant contrast enhancement.

The target-containing DsRed cells demonstrated a slightly higher cellular relaxation rate $R_{1,cell}$ for the antisense CA compared to the parent CCL-11 cells (Figure 5b). Whether a specific interaction between our anti-dsred CA and the cellular target mRNA was responsible for this observed effect remained unclear and is still under investigation. A decreased rotational correlation time and thus a greater τ_r effect was expected upon binding of antisense CA with DsRed2 mRNA (*44*). However, no such effect was observed even in the target-containing cells. In addition, no specific accumulation of the antisense CA in comparison to the nonsense CA could be detected in DsRed cells. Due to the predominantly endosomal uptake, a mainly unspecific accumulation could be observed. Additionally, the efflux from nontargeted cells would be disturbed and at least slowed down. These findings suggest that, although the CPP-PNA CAs efficiently permeate cells, their interaction with the target mRNA appears limited. This could arise due to the localization of the conjugates and the target in different cellular compartments.

Fluorescence Microscopy Studies. High-resolution microscopy was performed to elucidate the intracellular distribution of the FITC-containing CPP-PNA conjugates. DsRed cells were cultured in channel slides and labeled with antisense CA. After removal of surface-bound fluorescence by trypan blue and nuclear staining with Hoechst, cells were examined under the microscope. Confocal-like 3D image data were acquired using

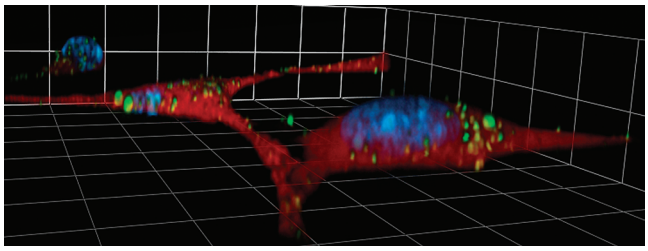

Figure 6. Endosomal localization of anti-dsred CA in DsRed cells. Cells were incubated with anti-dsred CA and cell nuclei were counterstained by Hoechst 33342. External fluorescence was quenched by trypan blue and subsequently washed with HBSS; DsRed CA, green (FITC fluorescence); nuclei, blue (Hoechst 33342). The 3D image was rendered from obtained 2D slices. A single unit represents 13.3 μm.

the OptiGrid Structured Illumination device that eliminates all out-of-focus information from the image (*45*). A high-speed Micro-Shutter was also integrated into the Zeiss microscope to control the exposure times and reduce sample photobleaching. Z-stacks were collected for a single time point using a multiple channel acquisition protocol. The combination of hardware and software used for microscopic evaluation was optimal for rapid and high-resolution observation of living cells with minimized damage to samples. 3D images were reconstructed from the 2D slice images thus obtained.

Examination of DsRed cells labeled with antisense CA in 3D clearly revealed encapsulation of green fluorescent CA in intracellular vesicles around the nucleus (Figure 6). Although the target mRNA cannot be visualized by microscopy, it is expected to be distributed mainly throughout the cytosol, as is the case with the red fluorescent DsRed2 protein itself. On the other hand, the CA seemed to be entering cells by endocytosis and subsequently entrapped in endosomal/lysosomal vesicles with little or no release into the cytosol. Hence, the absence of target binding in cells can be explained by the localization of both the antisense PNA and target mRNA in segregated compartments within the same cell.

As more information is obtained about the mechanism of cellular delivery by CPPs, it is becoming evident, as also reported by other groups, that endocytosis is the main route of trans-membrane movement (*46*−*48*). However, there is a lack of definitive evidence on the maintenance of functionality of the CPP-associated cargo once it is conveyed into cells. Some studies indicate successful PNA interaction with the target after being delivered by membrane-transducing peptides (*49*−*51*). Other studies indicate limited PNA binding with the target due to entrapment of PNA conjugates in endosomes (*52, 53*).

Another interesting observation was that subsequent to quenching with trypan blue no traces of green fluorescence binding to the cellular membrane were noticed (*31*). Trypan blue interacts with the aromatic groups on FITC, and therefore, the fluorophore in the extracellular environment as well as the FITC in cells with compromized cell membrane integrity becomes quenched. This justifies the use of this stain to efficiently eliminate extracellular and membrane-bound fluorescence. Microscopic examination also indicates that, because of the quenching step in our washing protocol, only the internalized probe signal is quantified by fluorescence spectroscopy.

Biodistribution Properties. Coupling of PNA with Gd-DOTA-CPP(FITC) more than doubles the size of the conjugate. Thus, it was important to investigate the mobility of this large molecule *in vivo.* Fluorescence studies performed 20 min after i.v. injection showed that within minutes the compound entered various organs via the bloodstream, and was by no means limited to the injection site (Table 1). The fluorescence observed in the liver and bladder was very high, and the exposure time for fluorescence images was reduced almost 3.5 times in comparison

Table 1. Biodistribution of the Antisense CA in Various Tissues Represented Qualitatively[a]

tissue	fluorescence intensity
liver	+++
urinary bladder	+++
kidney	++
spleen	++
lungs	+
heart	±
brain	−
blood	−

[a] Tissues from C57/BL6 mice were extracted 20 min after CA administration and tissue slices were assessed for antisense CA-related green fluorescence. Tissues from animals injected with saline alone served as control.

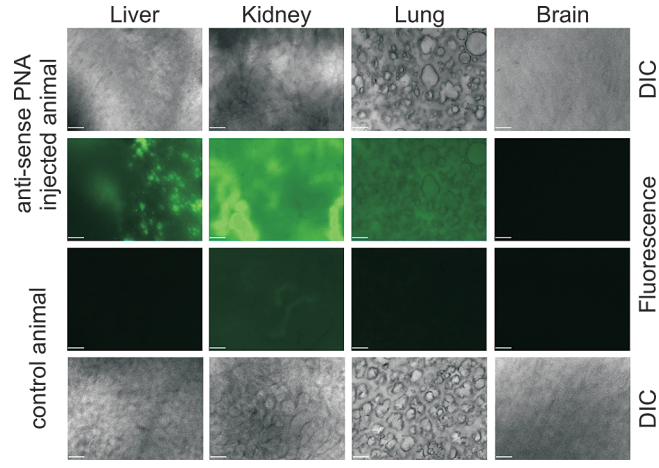

Figure 7. Distribution of anti-dsred CA in different tissues after *in vivo* labeling. Tissues were extracted 20 min after intravenous administration of anti-dsred CA to C57/BL6 mice. Fluorescence and bright field images of the tissues were obtained. For fluorescence images of liver, an exposure time of 175 ms was used, while for all other tissues, it was adjusted to 600 ms. The bar represents 160 μm.

to the rest of the tissues (Figure 7). The lipophilic nature of the PNA-containing CA explains the affinity of the conjugate for liver tissues. Kidneys and spleen were moderately labeled, whereas heart and lungs were only faintly fluorescent. Absolutely no penetration of the CA into the brain was detected, thus indicating a lack of penetration of the blood−brain barrier. Although these biodistribution studies are preliminary, they clearly indicate that the bulky PNA-containing antisense CA spontaneously disperses in the organism after injection and also rapidly enters the excretory system.

In conclusion, we report here the synthesis of a couple of cell-penetrating gadolinium-based conjugates, the most efficient of which was selected for coupling with PNA sequences. Both the PNA-CPP CAs labeled cells very well, regardless of whether they contained the specific target. mRNA targeting could not be realized; nevertheless, we have succeeded in generating highly efficient and nontoxic cell-internalizing and contrast-enhancing MR agents. Future studies need to be focused on the improvement of vesicular release after endocytosis or finding methods for direct cytosolic uptake and developing targeted contrast agents for better understanding of the mechanism of contrast enhancement at the cellular level.

ACKNOWLEDGMENT

The authors thank Dr. Marna Ericsson, University of Minnesota, for the generous gift of the DsRed2-transfected CCL-11 cell line. The authors especially acknowledge the help of Ms. Hildegard Schulz, High Field Magnetic Resonance Center,

Max Planck Institute for Biological Cybernetics, in carrying out these studies. This work was supported by the Max-Planck Society and was performed in the frame of COST action D38.

Supporting Information Available: Characterization data for the conjugates and gel retardation assay described. This material is available free of charge via the Internet at http://pubs.acs.org.

LITERATURE CITED

(1) Weissleder, R., and Mahmood, U. (2001) Molecular imaging. *Radiology 219*, 316–33.
(2) Doubrovin, M., Serganova, I., Mayer-Kuckuk, P., Ponomarev, V., and Blasberg, R. G. (2004) Multimodality in vivo molecular-genetic imaging. *Bioconjugate Chem. 15*, 1376–88.
(3) Willmann, J. K., van Bruggen, N., Dinkelborg, L. M., and Gambhir, S. S. (2008) Molecular imaging in drug development. *Nat. Rev. Drug Discovery 7*, 591–607.
(4) Massoud, T. F., and Gambhir, S. S. (2003) Molecular imaging in living subjects: seeing fundamental biological processes in a new light. *Genes Dev. 17*, 545–80.
(5) Min, J. J., and Gambhir, S. S. (2004) Gene therapy progress and prospects: noninvasive imaging of gene therapy in living subjects. *Gene Ther. 11*, 115–25.
(6) Merbach, A. E., and Toth, E. (2001) *The Chemistry of Contrast Agents in Medical Magnetic Resonance Imaging*, John Wiley and Sons, New York.
(7) Aime, S., Cabella, C., Colombatto, S., Geninatti Crich, S., Gianolio, E., and Maggioni, F. (2002) Insights into the use of paramagnetic Gd(III) complexes in MR-molecular imaging investigations. *J. Magn. Reson. Imaging 16*, 394–406.
(8) Weinmann, H. J., Ebert, W., Misselwitz, B., and Schmitt-Willich, H. (2003) Tissue-specific MR contrast agents. *Eur. J. Radiol. 46*, 33–44.
(9) Karabulut, N., and Elmas, N. (2006) Contrast agents used in MR imaging of the liver. *Diagn. Interv. Radiol. 12*, 22–30.
(10) Artemov, D., Mori, N., Okollie, B., and Bhujwalla, Z. M. (2003) MR molecular imaging of the Her-2/neu receptor in breast cancer cells using targeted iron oxide nanoparticles. *Magn. Reson. Med. 49*, 403–8.
(11) Artemov, D., Mori, N., Ravi, R., and Bhujwalla, Z. M. (2003) Magnetic resonance molecular imaging of the HER-2/neu receptor. *Cancer Res. 63*, 2723–7.
(12) Towner, R. A., Smith, N., Doblas, S., Tesiram, Y., Garteiser, P., Saunders, D., Cranford, R., Silasi-Mansat, R., Herlea, O., Ivanciu, L., Wu, D., and Lupu, F. (2008) In vivo detection of c-Met expression in a rat C6 glioma model. *J. Cell Mol. Med. 12*, 174–86.
(13) Wang, Z. J., Boddington, S., Wendland, M., Meier, R., Corot, C., and Daldrup-Link, H. (2008) MR imaging of ovarian tumors using folate-receptor-targeted contrast agents. *Pediatr. Radiol. 38*, 529–37.
(14) Lee, J., Burdette, J. E., MacRenaris, K. W., Mustafi, D., Woodruff, T. K., and Meade, T. J. (2007) Rational design, synthesis, and biological evaluation of progesterone-modified MRI contrast agents. *Chem. Biol. 14*, 824–34.
(15) Heckl, S., Pipkorn, R., Waldeck, W., Spring, H., Jenne, J., von der Lieth, C. W., Corban-Wilhelm, H., Debus, J., and Braun, K. (2003) Intracellular visualization of prostate cancer using magnetic resonance imaging. *Cancer Res. 63*, 4766–72.
(16) Su, W., Mishra, R., Pfeuffer, J., Wiesmuller, K. H., Ugurbil, K., and Engelmann, J. (2007) Synthesis and cellular uptake of a MR contrast agent coupled to an antisense peptide nucleic acid--cell- penetrating peptide conjugate. *Contrast Media Mol. Imaging 2*, 42–9.
(17) Lindgren, M., Hallbrink, M., Prochiantz, A., and Langel, U. (2000) Cell-penetrating peptides. *Trends Pharmacol. Sci. 21*, 99–103.
(18) Kersemans, V., Kersemans, K., and Cornelissen, B. (2008) Cell penetrating peptides for in vivo molecular imaging applications. *Curr. Pharm. Des. 14*, 2415–47.
(19) Derossi, D., Chassaing, G., and Prochiantz, A. (1998) Trojan peptides: the penetratin system for intracellular delivery. *Trends Cell Biol. 8*, 84–7.
(20) Mae, M., and Langel, U. (2006) Cell-penetrating peptides as vectors for peptide, protein and oligonucleotide delivery. *Curr. Opin. Pharmacol. 6*, 509–14.
(21) Howl, J., Nicholl, I. D., and Jones, S. (2007) The many futures for cell-penetrating peptides: how soon is now? *Biochem. Soc. Trans. 35*, 767–9.
(22) Zorko, M., and Langel, U. (2005) Cell-penetrating peptides: mechanism and kinetics of cargo delivery. *Adv. Drug Delivery Rev. 57*, 529–45.
(23) El-Andaloussi, S., Jarver, P., Johansson, H. J., and Langel, U. (2007) Cargo-dependent cytotoxicity and delivery efficacy of cell-penetrating peptides: a comparative study. *Biochem. J. 407*, 285–92.
(24) Wacnik, P. W., Baker, C. M., Herron, M. J., Kren, B. T., Blazar, B. R., Wilcox, G. L., Hordinsky, M. K., Beitz, A. J., and Ericson, M. E. (2005) Tumor-induced mechanical hyperalgesia involves CGRP receptors and altered innervation and vascularization of DsRed2 fluorescent hindpaw tumors. *Pain 115*, 95–106.
(25) Sarin, V. K., Kent, S. B., Tam, J. P., and Merrifield, R. B. (1981) Quantitative monitoring of solid-phase peptide synthesis by the ninhydrin reaction. *Anal. Biochem. 117*, 147–57.
(26) Paull, B., and Haddaad, P. R. (1999) Chelation ion chromatography of trace metal ions using metallochromic ligands. *Trends Anal. Chem. 18*, 107–114.
(27) Aarons, R. J., Notta, J. K., Meloni, M. M., Feng, J., Vidyasagar, R., Narvainen, J., Allan, S., Spencer, N., Kauppinen, R. A., Snaith, J. S., and Faulkner, S. (2006) A luminescent probe containing a tuftsin targeting vector coupled to a terbium complex. *Chem. Commun. (Camb.)* 909–11.
(28) Kelly, K. A., Reynolds, F., Weissleder, R., and Josephson, L. (2004) Fluorescein isothiocyanate-hapten immunoassay for determination of peptide-cell interactions. *Anal. Biochem. 330*, 181–5.
(29) Richards, W. L., Song, M. K., Krutzsch, H., Evarts, R. P., Marsden, E., and Thorgeirsson, S. S. (1985) Measurement of cell proliferation in microculture using Hoechst 33342 for the rapid semiautomated microfluorimetric determination of chromatin DNA. *Exp. Cell Res. 159*, 235–46.
(30) Blaheta, R. A., Franz, M., Auth, M. K., Wenisch, H. J., and Markus, B. H. (1991) A rapid non-radioactive fluorescence assay for the measurement of both cell number and proliferation. *J. Immunol. Methods 142*, 199–206.
(31) Rennert, R., Wespe, C., Beck-Sickinger, A. G., and Neundorf, I. (2006) Developing novel hCT derived cell-penetrating peptides with improved metabolic stability. *Biochim. Biophys. Acta 1758*, 347–54.
(32) Gammon, S. T., Villalobos, V. M., Prior, J. L., Sharma, V., and Piwnica-Worms, D. (2003) Quantitative analysis of permeation peptide complexes labeled with Technetium-99m: chiral and sequence-specific effects on net cell uptake. *Bioconjugate Chem. 14*, 368–76.
(33) Wender, P. A., Mitchell, D. J., Pattabiraman, K., Pelkey, E. T., Steinman, L., and Rothbard, J. B. (2000) The design, synthesis, and evaluation of molecules that enable or enhance cellular uptake: peptoid molecular transporters. *Proc. Natl. Acad. Sci. U.S.A. 97*, 13003–8.
(34) Allen, M. J., MacRenaris, K. W., Venkatasubramanian, P. N., and Meade, T. J. (2004) Cellular delivery of MRI contrast agents. *Chem. Biol. 11*, 301–7.
(35) Jones, S. W., Christison, R., Bundell, K., Voyce, C. J., Brockbank, S. M., Newham, P., and Lindsay, M. A. (2005) Characterisation of cell-penetrating peptide-mediated peptide delivery. *Br. J. Pharmacol. 145*, 1093–102.
(36) Bhorade, R., Weissleder, R., Nakakoshi, T., Moore, A., and Tung, C. H. (2000) Macrocyclic chelators with paramagnetic cations are internalized into mammalian cells via a HIV-tat

derived membrane translocation peptide. *Bioconjugate Chem. 11*, 301–5.
(37) Prantner, A. M., Sharma, V., Garbow, J. R., and Piwnica-Worms, D. (2003) Synthesis and characterization of a Gd-DOTA-D-permeation peptide for magnetic resonance relaxation enhancement of intracellular targets. *Mol. Imaging 2*, 333–41.
(38) Bullok, K. E., Dyszlewski, M., Prior, J. L., Pica, C. M., Sharma, V., and Piwnica-Worms, D. (2002) Characterization of novel histidine-tagged Tat-peptide complexes dual-labeled with (99m)Tc-tricarbonyl and fluorescein for scintigraphy and fluorescence microscopy. *Bioconjugate Chem. 13*, 1226–37.
(39) Wright, L. R., Rothbard, J. B., and Wender, P. A. (2003) Guanidinium rich peptide transporters and drug delivery. *Curr. Protein Pept. Sci. 4*, 105–24.
(40) Shakeel, S., Karim, S., and Ali, A. (2006) Peptide Nucleic Acids (PNA) - a review. *J. Chem. Technol. Biotechnol. 81*, 892–899.
(41) Oehlke, J., Wallukat, G., Wolf, Y., Ehrlich, A., Wiesner, B., Berger, H., and Bienert, M. (2004) Enhancement of intracellular concentration and biological activity of PNA after conjugation with a cell-penetrating synthetic model peptide. *Eur. J. Biochem. 271*, 3043–9.
(42) Woolf, T. M., Melton, D. A., and Jennings, C. G. (1992) Specificity of antisense oligonucleotides in vivo. *Proc. Natl. Acad. Sci. U.S. A. 89*, 7305–9.
(43) Endres, P. J., Macrenaris, K. W., Vogt, S., and Meade, T. J. (2008) Cell-permeable MR contrast agents with increased intracellular retention. *Bioconjugate Chem*.
(44) Zech, S. G., Eldredge, H. B., Lowe, M. P., and Caravan, P. (2007) Protein binding to lanthanide(III) complexes can reduce the water exchange rate at the lanthanide. *Inorg. Chem. 46*, 3576–84.
(45) Neil, M. A., Juskaitis, R., and Wilson, T. (1997) Method of obtaining optical sectioning by using structured light in a conventional microscope. *Opt. Lett. 22*, 1905–7.
(46) Chauhan, A., Tikoo, A., Kapur, A. K., and Singh, M. (2007) The taming of the cell penetrating domain of the HIV Tat: myths and realities. *J. Controlled Release 117*, 148–62.
(47) Gump, J. M., and Dowdy, S. F. (2007) TAT transduction: the molecular mechanism and therapeutic prospects. *Trends Mol. Med. 13*, 443–8.
(48) Futaki, S., Nakase, I., Tadokoro, A., Takeuchi, T., and Jones, A. T. (2007) Arginine-rich peptides and their internalization mechanisms. *Biochem. Soc. Trans. 35*, 784–7.
(49) Jia, F., Figueroa, S. D., Gallazzi, F., Balaji, B. S., Hannink, M., Lever, S. Z., Hoffman, T. J., and Lewis, M. R. (2008) Molecular imaging of bcl-2 expression in small lymphocytic lymphoma using ^{111}In-labeled PNA-peptide conjugates. *J. Nucl. Med. 49*, 430–8.
(50) Tripathi, S., Chaubey, B., Ganguly, S., Harris, D., Casale, R. A., and Pandey, V. N. (2005) Anti-HIV-1 activity of anti-TAR polyamide nucleic acid conjugated with various membrane transducing peptides. *Nucleic Acids Res. 33*, 4345–56.
(51) Morris, M. C., Chaloin, L., Choob, M., Archdeacon, J., Heitz, F., and Divita, G. (2004) Combination of a new generation of PNAs with a peptide-based carrier enables efficient targeting of cell cycle progression. *Gene Ther. 11*, 757–64.
(52) Abes, S., Williams, D., Prevot, P., Thierry, A., Gait, M. J., and Lebleu, B. (2006) Endosome trapping limits the efficiency of splicing correction by PNA-oligolysine conjugates. *J. Controlled Release 110*, 595–604.
(53) Turner, J. J., Ivanova, G. D., Verbeure, B., Williams, D., Arzumanov, A. A., Abes, S., Lebleu, B., and Gait, M. J. (2005) Cell-penetrating peptide conjugates of peptide nucleic acids (PNA) as inhibitors of HIV-1 Tat-dependent trans-activation in cells. *Nucleic Acids Res. 33*, 6837–49.

BC9000454